Erratum

Erratum to "X-ray, heat excess and ^{4}He in the D/Pd system" [J. Electroanal. Chem. 435 (1997) 113][1]

D. Gozzi [a], F. Cellucci [a], L. Cignini [a], G. Gigli [a], M. Tomellini [a], E. Cisbani [b], S. rullani [b], G.M. Urciuoli [b]

[a] *Dipartimeno di Chimica, Università di Roma La Sapienza, P. le Aldo Moro 5, 00185 Roma, Italy*
[b] *Laboratorio di Fisica, Istituto Superiore di Sanità, V. le Regina Margherita 299, 00161 Roma, Italy*

The publisher regrets that this paper was printed with a number of errors. A correct version of the paper is printed below.

X-ray, heat excess and ^{4}He in the D/Pd system

D. Gozzi [a,*], F. Cellucci [1], P.L. Cignini[1], G. Gigli [a], M. Tomellini [2], E. Cisbani [3], S. Frullani [b], G.M. Urciuoli[3]

[a] *Dipartimeno di Chimica, Università di Roma La Sapienza, P. le Aldo Moro 5, 00185 Roma, Italy*
[b] *Laboratorio di Fisica, Istituto Superiore di Sanità, V. le Regina Margherita 299, 00161 Roma, Italy*

Abstract

The energy balance between heat excess and ^{4}He in the gas phase has been found to be reasonably satisfied even if the low levels of ^{4}He do not give the necessary confidence to state definitely that we are dealing with the fusion of deuterons to give ^{4}He. In the melted cathode, the data of which are reported, no ^{4}He was found at the achieved sensitivity. X-ray film, positioned at 50 mm from the cell, roughly gave the image of the cathode through spots. Extended considerations have been made to explain this evidence on the basis of the bundle nature of the cathode. From these considerations, the energy of the radiation and the total energy associated to it have been extimated as 89 keV and 12 kJ, respectively. This value is $\approx 0.5\%$ of the energy measured by calorimetry in the same interval of time. The highest values of energy and excess power are 8.3 MJ and 10 W, respectively. © 1998 Elsevier Science S.A. All rights reserved.

1. Introduction

The debate on the anomalous behaviour of the system Pd-D is still open because, in spite of the intense research activity over the last seven years in many laboratories worldwide, a clear-cut picture of all the evidence claimed is still lacking. Since 1989 [1], many technical papers have been published [2]; 21 conference proceedings have been published on this subject, more than 200 patents have been issued, some promising theories have been proposed, but, form an experimental point of view, the crucial initial point—the energy balance, has not yet found a satisfactory and convincing explanation. All the efforts made to explain the

excess heat found as to chemical nature have been considered meaningless so far, because no chemical reaction we can imagine, in the environment where the experiments of deuterium confinement generally occur, is suitable to yield comparable amounts of heat. The whole situation, restricted only to the heat excess findings, easily leads to the following consideration: either heat excess measurements are all experimental artefacts, or we are dealing with new phenomena. By examining the abundant literature and some critical revisions [3], and through our direct experience gained in the field [4–6], the evidence is unconvincing and weak to support the hypothesis that we are in the presence of a collective worldwide mistake in measuring the heat excess. Several laboratories, using different techniques and protocols, found the same phenomenology and comparable results even if the reproducibility and full control of the experiments are still lacking. On the other hand, many experiments show other phenomena associated with the heat excess production, the source of which does not seem reasonably to be based on chemistry: emission of X-rays [7–9], as it will be shown

in this paper, and neutrons [10–13], as well as production of ^{4}He [14–17] and ^{3}H [6,18–21]. Unfortunately, in these experiments, the measured intensity of the radiation and number of particles is so low that the confidence in the detection statistics is always questioned. Despite this, there are a sufficiently large number of high-quality excess heat, particle and radiation measurements that are intriguing, suggesting that what has been measured and reported since 1989 is not an *ensemble* of mistakes and artefacts. Can a simple physico-chemical process, like the insertion of deuterium into the Pd lattice, whose energy is ≈ 0.1 eV/cm^3, produce X-ray emission or other nuclear products at tenths of keV or some MeV? The answer is: based on the chemistry we know, NO! But the explanation is hart to find anywhere in our current knowledge of physics. The very low energy of the particles in the solid state, the Coulomb barrier, very low cross-sections of possible nuclear reactions, etc. are very strong arguments to support skepticism and criticism. This paper reports on our most recent experiments on the electrochemical confinement of deuterium in palladium. The experimental results presented here come from the most complex and complete experiments that we have conducted since our first work in 1989.

2. Experimental

A detailed description of the entire experimental set-up is given elsewhere [5,6]. New features added or modified since our last published work are described.

2.1. Electrochemical and calorimetric cell

The Pyrex stainless steel cell, Fig. 1, is designed to accomplish the following tasks: (i) to avoid any ^{4}He contamination (^{4}He content in air is 5.24 ppm) of the escaping electrolysis gases in which ^{4}He is to be measured online (this is obtained by a high-vacuum tested SS holder containing the part of the cell emerging from the thermostatic bath. A stream of ^{4}He free boiling-off LN$_2$ circulates inside and outside the cell at 35 std cm^3 mm^{-1} and 2.25 bar); (ii) to be a flow-calorimeter in which the circulating water can exchange heat only with the electrolytic solution (this is produced by two jackets external to the pyrex tube containing the electrolyte solution. The inntermost jacket is used for the circulation of doubly distilled water at constant flow rate, and the outermost one is sealed under high vacuum and it is mirror-like on the top to minimze the leakage of heat by radiation); (iii) to maintain constant the level of the electrolyte through an optoelectronic sensor controlling the feed of D$_2$O which is consumed during the experiment by the electrolysis, according to Faraday's law, and evaporation; (iv) to perform in situ heat calibra-

tions through an internal resistor. At the stationary state, the energy balance of the cell is given by the equation below as:

$$P_{el} + P_{cal} + P_{exc} = P_w + P_{rad} + P_{sg} \tag{1}$$

where el is the electric power applied to carry out the electrolysis; cal is the power through the internal heat for making in situ calibrations; exc is the power in excess to be measured; w is the power exchanged by the water stream crossing the innermost jacket; rad is the power radiated from the cell toward the bath; and sg is the power necessary to saturate with D$_2$O vapor the gas stream that is composed of the protective gas N$_2$ and electrolysis gases D$_2$ and O$_2$. Its composition, at fixed N$_2$ flow rate, q_{N_2}, depends on the electrolysis current I. At $t > \tau$, the time constant of the cell (see Eq. (2)), through Eq. (1), would allow P_{exc} to be calculated [6]:

$$P_{exc} + V_h I_h + (V_{in} - V_{th})I$$
$$= (\rho c_1 q)_{H_2O} \Delta \vartheta_{wj,\infty} + k_{Rad} S_s \{[\vartheta_{tb} + \Delta \vartheta_{wj,\infty}]^4 - \vartheta_{tb}^4\}$$
$$+ \left(\frac{3I}{4F} + \frac{P}{R\vartheta_r} q_{N_2}\right) \left[\frac{p(\vartheta_s)}{P - p(\vartheta_s)}\right]$$
$$\times [(C_g - C_1)_{D_2O}\vartheta_s + \lambda_{D_2O}] \tag{2}$$

Eq. (2) can be used provided the temperature difference, $\Delta \vartheta_{wj,\infty}$, at the inlet and outlet of the water cooled jacket, the temperature of the bath, ϑ_{tb}, the cooling water flow rate, q, the potential drop, $V_{in}(I)$ at the electrodes, the room temperature, ϑ_r, the temperature of the solution, ϑ_s, the total pressure P are measured during the experiment. $p(\vartheta_S)$ is the vapor pressure of the solution at temperature ϑ_s. Λ_{D_2O}, C_g, and C_1 are quantities referred to D$_2$O, the heat of evaporation, and heat capacity of gas and liquid, respectively. V_{th} is the thermoneutral potential (1.5367 V) [22] for the decomposition of D$_2$O and the product $V_h I_h$ is the input power applied to the internal resistor when the calibration step is on. S_s is the radiating surface area of the cell and k_{Rad} the Stefan–Boltzmann constant. However, instead of using Eq. (2), it is common practice to perform the calibration of the cell both before starting the electrolysis and in progress by making use of the internal heater. A detailed discussion of the use of the heater pulses for measuring the excess heat power is given in Appendix A.

Fig. 2A shows the typical response of a blank cell (Pt cathode implies that $P_{exc} = 0$) when step-fashion variations of the input power (right scale) are applied to it. In Fig. 2B, we have the superimposition of power generated by the internal heater, P_{cal}, and a constant thermal power, P_{el}, generated by electrolysis, $P_{in} = P_{cal} + P_{el}$. The stationary values of $\Delta \vartheta_{wj,\infty}$ vs. the input power are reported in Fig. 2C for the four cells under test. A set of these values represent the calibration. The different slopes are connected to the different flow rates
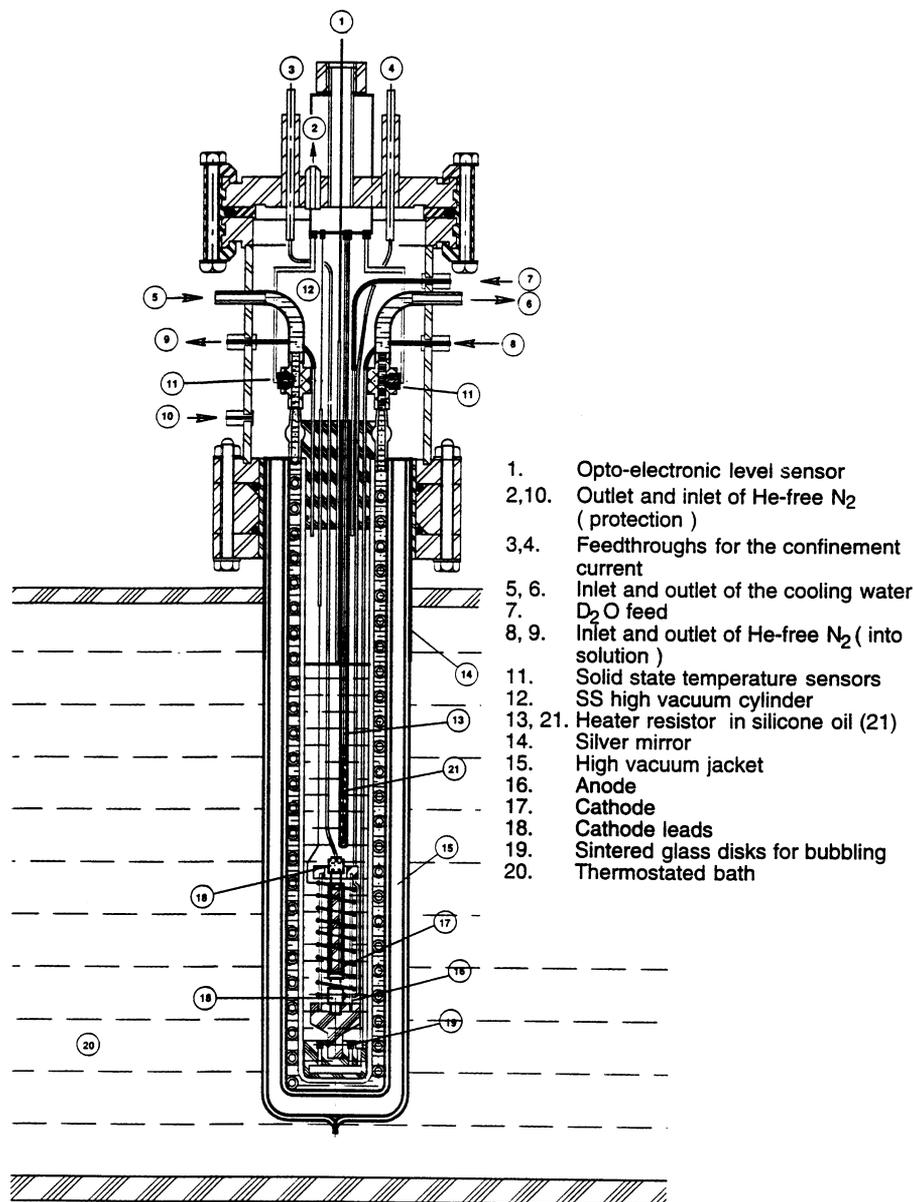
Fig. 1. New cell design.

1. Opto-electronic level sensor
2,10. Outlet and inlet of He-free N_2 (protection)
3,4. Feedthroughs for the confinement current
5, 6. Inlet and outlet of the cooling water
7. D_2O feed
8, 9. Inlet and outlet of He-free N_2 (into solution)
11. Solid state temperature sensors
12. SS high vacuum cylinder
13, 21. Heater resistor in silicone oil (21)
14. Silver mirror
15. High vacuum jacket
16. Anode
17. Cathode
18. Cathode leads
19. Sintered glass disks for bubbling
20. Thermostated bath

of water in the water jacket, wj, as reported in Table 1. As a first approximation, by neglecting the second and third terms of the right side of Eq. (2), one obtains:

$$P_{in} = (\rho c_1 q)_{wj} \Delta\vartheta_{wj,\infty} \qquad (3)$$

where the slope of the curve $P_{in}/\Delta\vartheta_{wj,\infty}$ vs. q_{wj} depends only on constant terms, $(\rho c_1)_{wj} = 4.172$ J cm^{-3} °C^{-1} at 21°C. The value 4.6 ± 0.1 J cm^{-3} °C^{-1} was found as average value on the four cells under test.

The straight-line behaviour of the calibration curves shows that the second and third terms of the right side of Eq. (2) are either negligible, or their sum is linear also. This is what one finds for the terms P_{rad} and P_{sg} by using [6]: $I = 1$ A, $S_s = 240$ cm^2, $\vartheta_{tb} = 21$°C, $\vartheta_r =$

30°C, $q_{N_2} = 5.8 \times 10^{-7}$ m^3 s^{-1} and $P = 2.25$ bar as typical values.

The time response of the cell is well-described by the differential equation below:

$$\Delta\vartheta_{wj} + \left(\frac{q}{v}\right)_{wj} \Delta\vartheta_{wj} - \frac{P_\Sigma}{(\rho c_l v)_{wj}} = 0 \qquad (4)$$

in which the terms of P_{rad} and P_{sg} are considered negligible and P_Σ is the sum of all the terms of the left side of Eq. (1). v_{wj} is the volume of water contained in the water jacket between the inlet and outlet temperature sensors (see Fig. 1). The integral of Eq. (4) gives the time dependence of $\Delta\vartheta_{wj}$ according to the equation:

$$\Delta\vartheta_{wj}(t) = \frac{P_\Sigma}{(\rho c_1 q)_{wj}} - \left[\frac{P_\Sigma}{(\rho c_1 q)_{wj}} - \Delta\vartheta_{wj,t=0}\right] e^{-t/\tau} \qquad (5)$$

where $\tau = \left(\dfrac{v}{q}\right)_{wj}$. For $t \gg \tau$, $\Delta\vartheta_{wj}(t) = \dfrac{P_\Sigma}{(\rho c_1 q)_{wj}} = \Delta\vartheta_{wj,\infty}$ which is consistent with Eq. (3). Through a plot of the quantity $\ln f(\Delta\vartheta_{wj}) = (\Delta\vartheta_{wj}(t) - \Delta\vartheta_{wj,\infty})/\Delta\vartheta_{wj,t=0} - \Delta\vartheta_{wj,\infty}$ versus t, the time constant was obtained as given in Fig. 3. As shown, the time constant of the cell is a function of the flow rate of the cooling water so that, by increasing the flow rate, the time constant decreases but this makes the sensitivity (the slope of the calibration curve) poorer.

Table 1
Calibration curves given by the best fitting equation = $\Delta\vartheta_{wj,\infty} = (a \pm \Delta a) + (b \pm \Delta b)P_{in}$

Cell #	$(a \pm \Delta a)$ (°C)	$(b \pm \Delta b)$ (°C W^{-1})	R	Flow rate (cm^3 s^{-1})
1 (blank)	0.02 ± 0.01	0.118 ± 0.001	0.99944	1.9 (2.03)
2	0.00 ± 0.03	0.104 ± 0.002	0.99736	2.1 (2.31)
3	-0.09 ± 0.04	0.144 ± 0.003	0.99738	1.5 (1.67)
4	-0.048 ± 0.009	0.0871 ± 0.0007	0.99965	2.5 (2.75)

The flow rate in brackets are the expected values calculated as $q = \dfrac{1}{\rho c_1 b}$.

2.1.1. Electrodes

All the anodes were made of pure platinum from Engelhard and shaped as gauze cylinders having skeletons of 1 mm-diameter wires supporting the spot-welded mesh of 0.35 mm-diameter Pt wire. The mesh dimension was 5×4 mm^2 and the anode final size was 48 mm (height) and 12 mm (inside diameter). All the cathodes, except that of the blank cell, were made of pure palladium from Engelhard and shaped as bundles of wires wrapped at the ends by machined cylindrical pieces of 6-mm Pd rods. Each bundle was slightly rotated clockwise on its own axis. The overall external dimensions of the cathodes were 6-mm diameter × 55-mm height. The height of the bundle was 40 mm (only 24 mm were out of the wrapping) and its diameter was about 4 mm. Two out of three cathodes, belonging to the cells #3 and #4, were constituted by bundles of 150 wires of 250 μm diameter each and the other one, cell #2, by 42 wires of 500 μm. The cathode of the blank cell (cell #1) was shaped similarly but the bundle was formed by 10 Pt wires of 1 mm diameter and wrapped by using SS machined caps. All the cathodes were annealed in high vacuum at 970°C for 24 h and cooled at room temperature at a rate of 1°C/min.
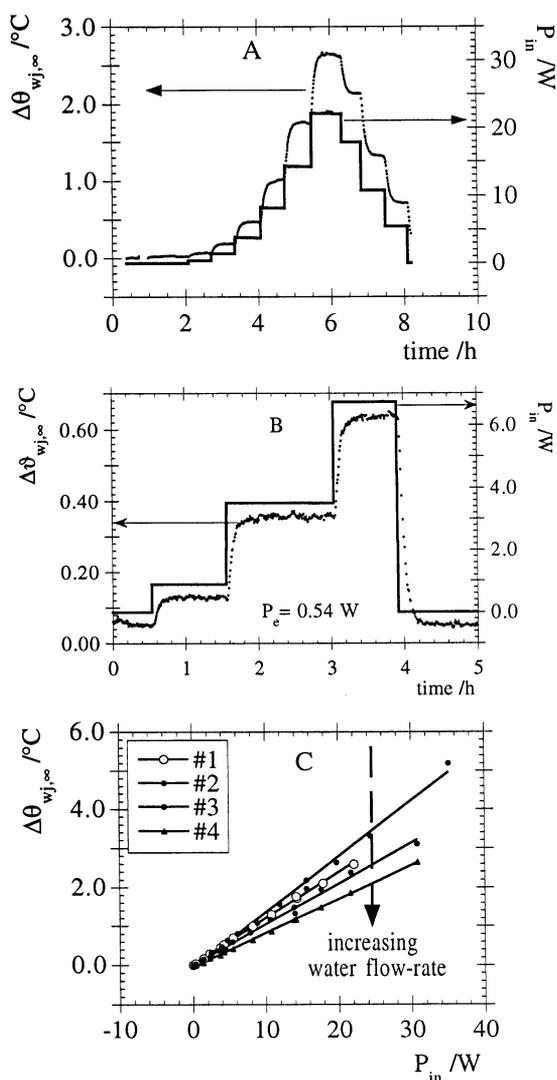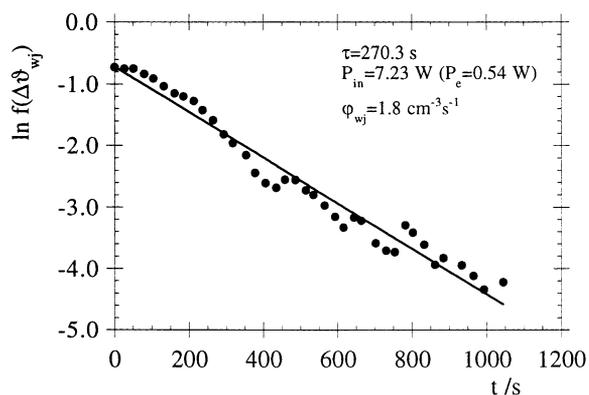

Fig. 2. (A) Response of the cell at step variations of input power generated by the internal heater; (B) Response of the cell at step variations of input power generated by the internal heater while electrolysis is running; (C) Calibration curves of the four cells under test.

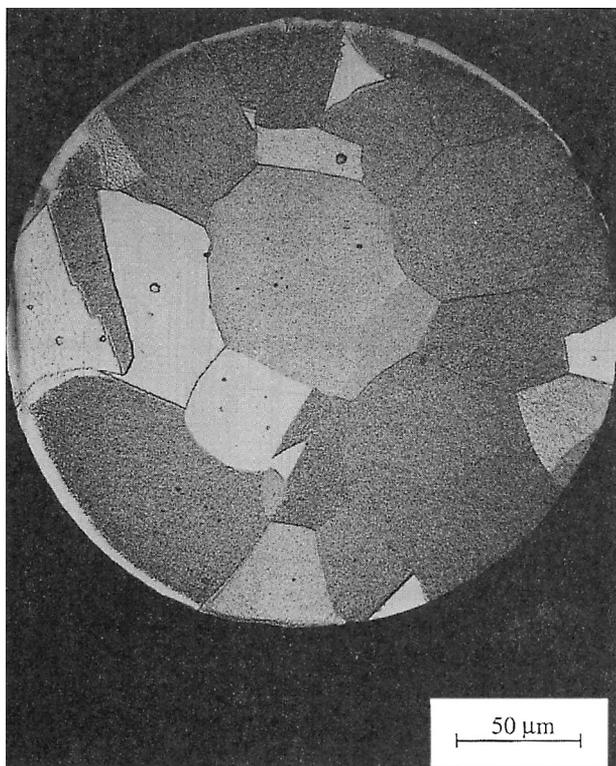Fig. 3. Determination of the time constant of the calorimeter cell.

Fig. 4. Microphotography of the cross-section of a 250-μm diameter wire of Pd after heat treatment.

This procedure greatly reduces internal stresses and dislocation concentration, allowing for the growth of large grains as was shown by metallographic analysis (see Fig. 4), which gave a 2D grain size distribution centred at 35 ± 5 μm (≈ 53 μm in 3D) [23].

2.2. X-ray detection

X-ray films (Kodak, type TM H/RA-1 19×24 cm^2) were used to detect emission from the cells. Before use, the film was inserted in a black plastic bag in a dark room and put in front of the cell at a 5-cm (see Table 2) distance as reported in Fig. 5. It is important to point out that the films were not in direct contact either with

Table 2
Materials interposed in between the cathode and X-ray film

Material	Thickness/cm	Density/g cm^{-3}
D$_2$O (LiOD)	1.25—$\phi/2$	1.104
Pyrex + coil	0.3	2.24
H$_2$O in coil	0.3	0.997
Pyrex + coil	0.3	2.24
Vacuum	0.8	0
Pyrex	0.2	2.24
H$_2$O	1.5	0.997
Perspex	0.5	1.19
Distance from the centre of the cathode	5.15—$\phi/2$	

ϕ is the cathode diameter (0.4–0.5 cm).

any part of the cell or with chemicals. Therefore, any damage of the film producing apparent traces or spots was avoided. The analysis of the film was carried out by midrodensitometer by steps of 600 μm along the Z-axis making at each step a scan of the X-axis by using a 50-μm slit. To convert he optical density data into exposure units (Roentgen), a calibration was done through known exposures of the same type of film (and using the same developing conditions) to the tungsten K$_\alpha$ radiation filtered by 0.5 mm Al.

2.3. High resolution mass spectrometry (HRMS)

2.3.1. In the gas stream coming out of the electrolytic cells

With respect to the previous procedure reported in the literature [14], some important improvements were brought to the ^{4}He determination in the electrolysis gas phase. In the present case, sampling and measurement are carried out online and this provides at least two great advantages: to avoid a potential source of contamination by atmospheric ^{4}He and to increase the number of measurements considerably. All this has been made possible by implementing the experiment with a high-resolution quadrupole mass spectrometer (Balzers QMS 421 gas tight crossbeam ion source and analyzer QMA 410) full PC-controlled and equipped with some features that allowed the automatic performance of several operations such as online sampling. The nominal mass range of QMS in HR mode is 27 amu.

All the tubings between the components of a line (cell, catalytic recombiner, automatic sampling system, gettering system, etc.) were made of SS tube 4 mm outer diameter (1.53 cm^3/m) and throughout the line, all the connections were of the Swagelock™ type. The Pyrex glass holder containing the catalytic recombiner is positioned inside a flanged SS cylinder where a stream of ^{4}He free boiling-off LN$_2$ circulates. Therefore, also in this case, the connections were of the Swagelock™ type. The sampling procedure for ^{4}He is performed after the deuterium removing system [6] has reduced the deuterium content of the gas mixture coming from the cell. The sampling apparatus and the related operations are illustrated in Fig. 6 and in the inset, respectively. A 150-cm^3 SS cylinder (one for each cell line), having a three-way electrovalve at both the ends, is in the normal position (a) flushed with the gas mixture is directed elsewhere to avoid overpressure on the line) and the outlet end is connected to an SS charcoal trap kept under vacuum and in LN$_2$. Then in phase (d), the cylinder sucks N$_2$ from a small tank connected to the LN$_2$ reservoir after that the electrovalves C, D, E have been switched on (c). When the pressure inside the tank becomes higher than the pressure of the line, N$_2$ is allowed to bubble again in the water (e) and then the line is connected to the cylinder ready for another
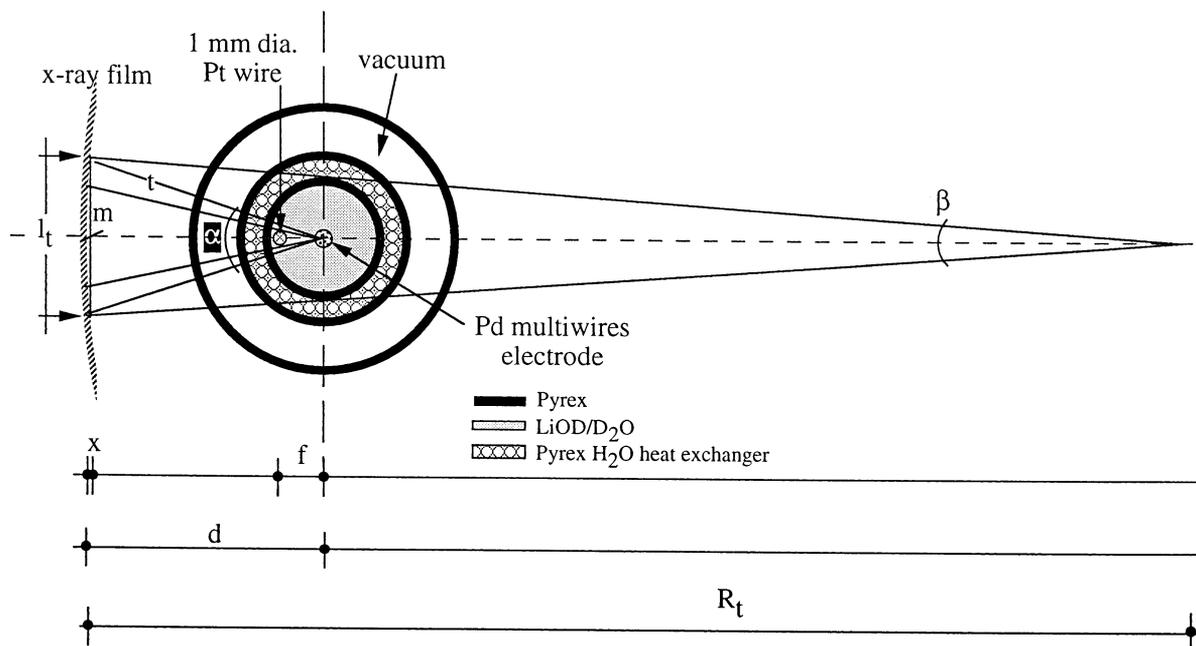
Fig. 5. Scheme of the positioning of the X-ray film in the experimental set-up. $R_t = 250$ mm is the radius of the torus containing the cells (see Fig. 8 of Ref. [6]). $d = 50$ mm and $f = 6.5$ mm. The materials in between the cell and film are given in Table 2.

sampling. The gas mixture trapped in the cylinder is allowed to be adsorbed in the LN_2 charcoal trap until the pressure becomes lower than a preset threshold (typically 5×10^{-2} mbar) then the injection of the gas mixture in the QMS chamber is realised.

HRMS measurements were carried out in multiple ion detection (MID) mode and the following ionic currents have been generally monitored for the species: $^4He^+$ (4.0026), valley $^4He-D_2$ (4.0111), D_2^+ (4.0282), $^{20}Ne^{2+}$ (9.996). The pressures in the QMS chamber, in the LN_2 trap and in the sampling cylinder were also monitored during each measurement. The software controls the samplings at a given interval of time (typically every 20 min), as well as each related measurement. The mass corresponding to the valley between $^4He-D_2$ is a key parameter for monitoring the complete separation between the two peaks of ^4He and D_2. This always occurs when the deuterium-removing system works properly. The presence of relevant quantities of deuterium with respect to ^4He makes its determination impossible. Reliable ^4He measurements could be obtained provided the ratio $D_2/^4He$ was lower than ≈ 3000. For the first time, the monitoring of $^{20}Ne^+$ was used by us in this kind of measurement [14] as the marker of a possible air contamination. It was also reported [14] that at around 20 amu, the mass spectra is complicated by the presence of several species that can compromise the use of such a marker. So the proposed monitoring of doubly ionized Ne [14], it is preferred here because, by making use of a MS with lower resolution, $^{20}Ne^{++}$ appears in a mass range without any relevant interference. Several calibrations made before and during the experiment, according

to a well-established procedure [14], were done to control the sensitivity, σ, of the QMS (see below). The equation: $Tat = 2.46 \times 10^{-2}c$ V_s holds between the absolute quantity of ^4He atoms in teratoms (10^{12} atoms) and their concentration in ppb in the gas mixture contained in the sampling volume V_s, given in cm³, at stp. This allows σ to be given in pA/Tat or in pA/ppb.

Measurements were made to establish the time behaviour of a ^4He parcel transported through the lines of the apparatus. The procedure was as follows: a known volume of air (10 std cm³ corresponding to 1.27×10^{15} ^4He atoms) was injected in one of the cells and, at fixed time delays, was sampled according to the previously described procedure, and a ^4He measurement was made. This was repeated for various time delays and the results are shown in Fig. 7. Throughout the procedure the flow rate of the boiling-off LN_2 was kept constant at 40 std cm³ min⁻¹ as then in the experiment. Fig. 7 shows the result obtained by such measurements that are fundamental to calculate the expected ^4He, at a certain time of sampling, by using the excess heat power measured at that time (see Appendix B).

It is important to point out that the chosen way to perform the sampling has the advantage of allowing the online detection of ^4He, where the risks of air contamination due to the offline samplings are avoided, even if this procedure implies that a large quantity of the gas mixture is lost. The ratio r_v between the volume of the gas mixture analysed V_a, in n samplings of an experiment last a time τ_e, and the volume of the gas mixture produced throughout the experiment, V_e is given by the equation:

to manifold

A

150 cm³ SS-cylinder

B

from line

to sampling panel

N₂ from LN₂ tank

C   **D**   **E**

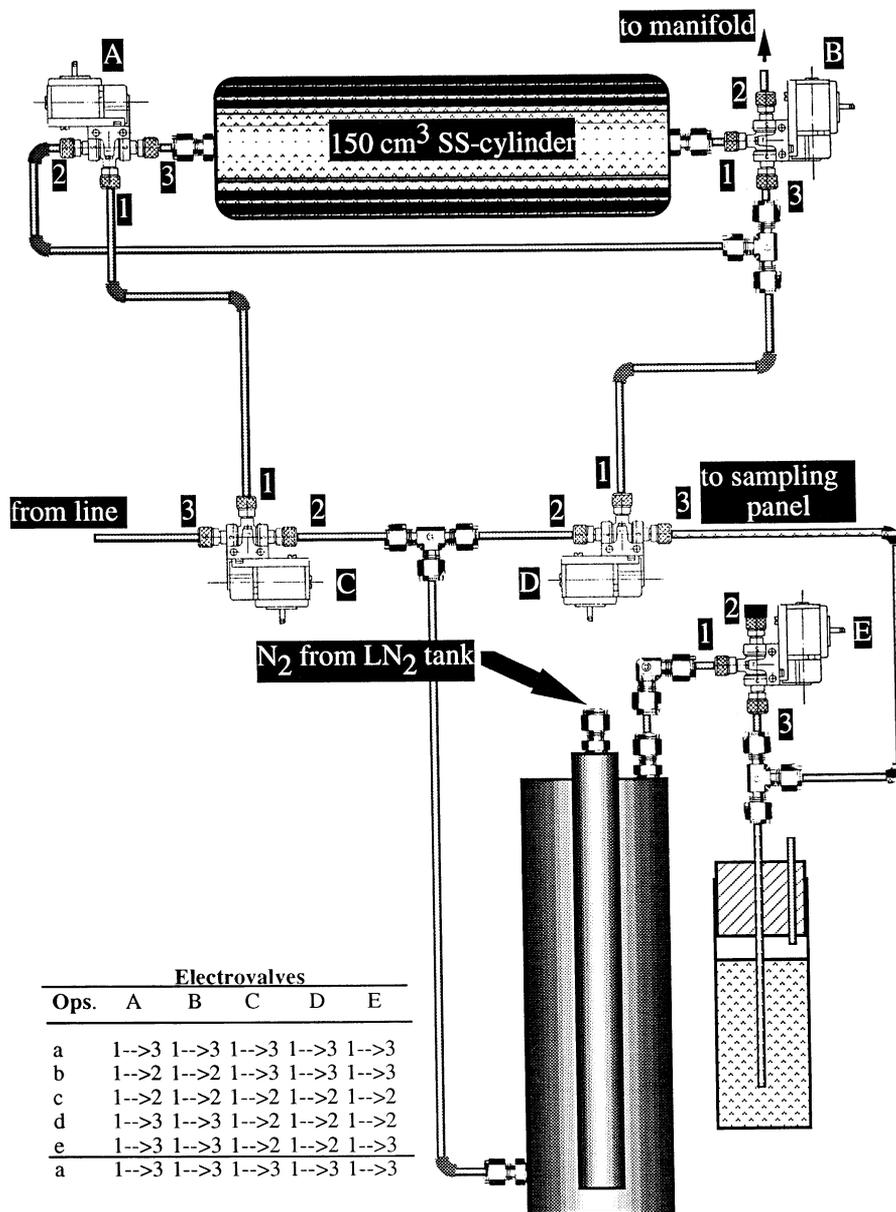| Ops.	Electrovalves				
	A	B	C	D	E
a	1-->3	1-->3	1-->3	1-->3	1-->3
b	1-->2	1-->2	1-->3	1-->3	1-->3
c	1-->2	1-->2	1-->2	1-->2	1-->2
d	1-->3	1-->3	1-->2	1-->2	1-->2
e	1-->3	1-->3	1-->2	1-->2	1-->3
a	1-->3	1-->3	1-->3	1-->3	1-->3

Fig. 6. Automatic online device for the sampling of the gas mixture.

$$r_v = \frac{V_a}{V_e} = \frac{nV_s}{q_m\tau_e} \tag{6}$$

where V_s is the volume of the sampling cylinder and q_m is the flow rate of the gas mixture

$$\left(q_m = \frac{3I}{4F} + \frac{P}{R\vartheta_r}q_{N_2}, \text{ see Eq. (2)}\right).$$

Optimization criteria and experimental needs limit the ability to increase r_v as much as would be desired. The main reason for this is the dependence of the mean sampling frequency n/τ_e on the gettering system and its regeneration time. For instance, for one of the cells, $n = 382$, $V_s = 150$ cm³, $\tau_e = 940$ h and $q_m \approx 45$ std cm³ min^{-1}, therefore, $r_v \cong 0.026$.

2.3.2. In the Pd electrodes

A homemade device was constructed to detect helium in the bulk of the Pd cathodes by making use of thermal desorption spectrometry (TDS). The experimental set-up, reported schematically in Fig. 8, is constituted by a high-vacuum pumping system connected to the heating chamber by a gate valve. The heating chamber is connected to the QMS through a gettering line for removing D_2 before the injection in the QMS. The heating element is a vertical cylinder-shaped tantalum foil 75 μm thick in which a graphite crucible is positioned. The samples, as cut sections of the cathodes, are stored in a multiple sample holder driven by an external manipulator. At fixed displacements of the manipulator, each sample is allowed to fall in the
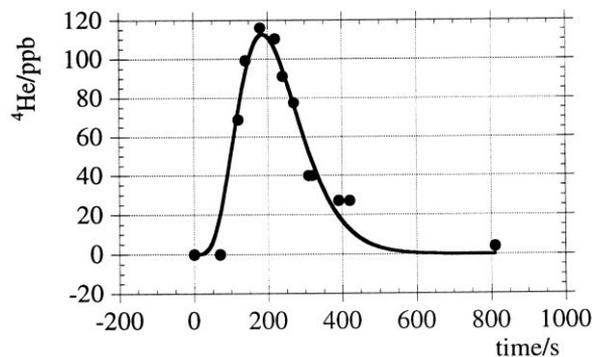
Fig. 7. Propagation of a *parcel* of ^{4}He in the line extending from the cell to the sampling cylinder after an injection in the cell of 10 scc of air (1.27×10^{15} ^{4}He atoms). Carrier gas flow rate = 40 sccm.

crucible. The standard procedure adopted here consists of heating the crucible over the m.p. of Pd (1552°C) under high-vacuum pumping; then, after closing the gate valve, make the samples fall into the crucible while increasing the temperature above 1650°C, and maintaining this temperature for at least 10 min. Finally a rapid cooling follows. At the same time, the evolved gases are allowed to be gettered, first in a LN_2 charcoal trap and, subsequently, by 57-707 SAES getters. Finally, when the pressure in the system decreases below 2×10^{-5} mbar, the QMS is connected and the measurement is carried out in MID mode.

3. Results

Figs. 9–12, for cells 1 to 4, respectively, show in the upper panels the total input power supplied to the cell
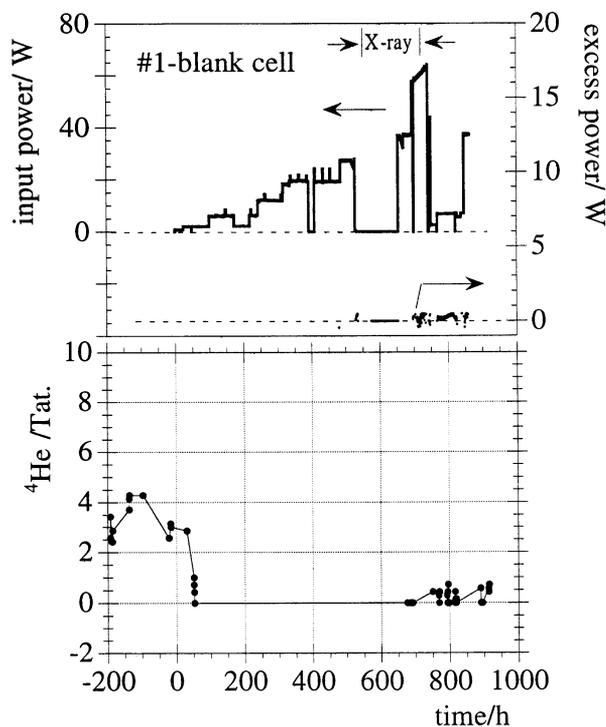

Fig. 9. Cell # 1 (blank). Cathode made of a bundle of 1 mm diameter Pt wires. Upper part: excess heat power (right scale) and total input power (left scale). Lower part: measured ^{4}He in teratoms. Each point is the absolute quantity of ^{4}He in the sampling volume of 150 cm^3.

(lefthand scale) and the time patterns for the excess heat power (righthand scale). The measured absolute quantity of ^{4}He in teratoms (10^{12} atoms) is given in the lower panels of each figure. The instability of the flow rate of the cooling water in some periods of the experiment prevented reliable data of excess heat power being
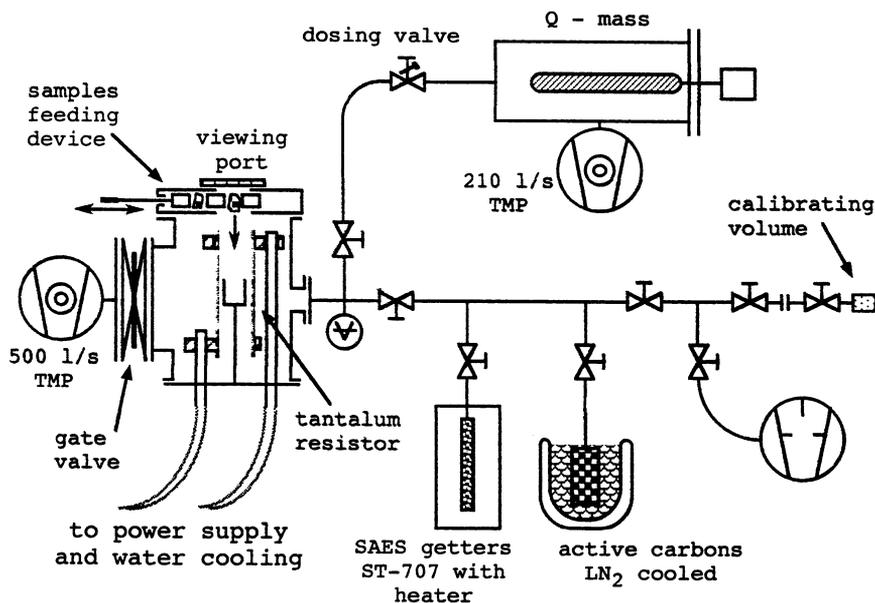

Fig. 8. Scheme of the apparatus for determining ^{4}He inside the cathode.

obtained. This is the reason why some parts of the plots do not show those data.

During the experiment, at ≈ 552 h since the starting of the electrolysis, an X-ray film was positioned in front of cell #4 and another one in front of the blank cell (#1) as reported, respectively, in Figs. 12 and 9. After an exposure of one week, the film related to the blank cell did not show any trace, whereas the other film showed several spots, roughly reproducing the image of the cathode. The film is reported in Fig. 13. The intensity, the dimensions and the coordinates of all the spots were measured according to Section 2, reported in Table 3 and plotted in Fig. 14. The spot diameter was found ranging from 0.41 to 2.45 mm. To be sure that no artefacts were occurring, a new film was inserted in the same black plastic bag and exposed to the light of the laboratory for some days. The film was found to be totally unexposed. The plane X, Z is the plane parallel to the film and the vertical axis at $X = 0$ coincides with the Z axis of the cathode, 50 mm far from the film.

After the experiment, the analysis of ^{4}He on some cut sections of the cathodes did not reveal any significant amount of ^{4}He embedded in the PdD$_x$ lattice over the detection limit of ~ 2 Tat as reported in Table 4 for cell #4.
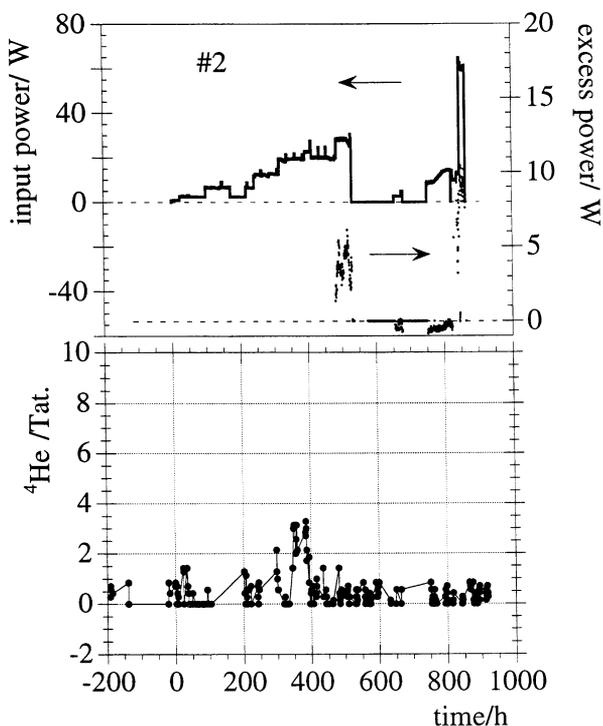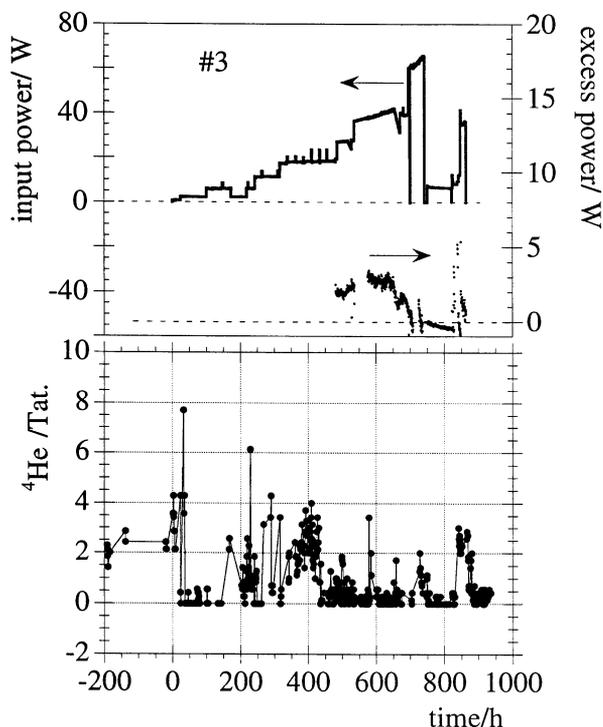

Fig. 11. Cell #3. Cathode made of a bundle of 250 μm diameter Pd wires. Upper part: excess heat power (right scale) and total input power (left scale). Lower part: measured ^{4}He in teratoms. Each point is the absolute quantity of ^{4}He in the sampling volume of 150 cm^3.

4. Discussion

4.1. Heat excess and helium-4

The ^{4}He measurements before the start of the electrolysis show that, after 200 h, from 1 (cell #2) to 3 (cell #1) Tat, 0.3 to 0.9 ppb, were still present although ^{4}He in boiling-off LN$_2$ is undetectable when measured directly at the outlet of the LN$_2$ reservoir. On the other hand, as each component of the lines was carefully tested for leaks and all the connections were realized with SS Swagelock fittings, we attribute that value to an incomplete washing of the whole line. This is also supported by several measurements made later on in the experiment which did not give any ^{4}He. At first glance, there is no direct time correlation between heat excess and ^{4}He (see, for instance, Fig. 12). However, it is important to remember that since the ^{4}He measurement is not performed in continuous mode, as is the heat power excess, a significant volume of the electrolysis gas mixture is lost without being analysed. To give some of the figures: about 2.24 m^3 at stp of gas mixture (mostly N$_2$, D$_2$, O$_2$) passed through the line but only 5.73×10^{-2} m^3 at stp were analysed in the 382 samplings (Fig. 12), 150 cm^3 each. This, according to Eq. (6), is less than 2.6%. Assuming that ^{4}He is formed at the surface, that is completely and instantaneously released in the gas phase and that the nuclear reaction

Fig. 10. Cell #2. Cathode made of a bundle of 500 μm diameter Pd wires. Upper part: excess heat power (right scale) and total input power (left scale). Lower part: measured ^{4}He in teratoms. Each point is the absolute quantity of ^{4}He in teratoms. Each point is the absolute quantity of ^{4}He in the sampling volume of 150 cm^3.
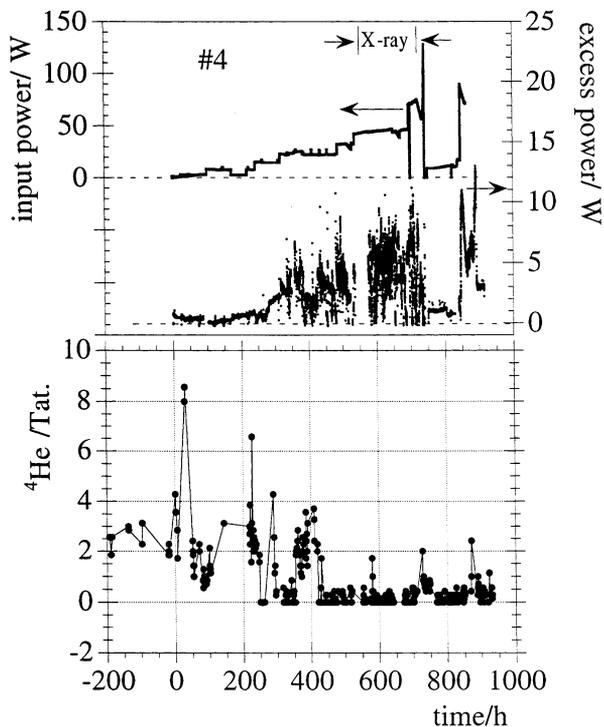
Fig. 12. Cell #4. Cathode made of a bundle of 250 μm diameter Pd wires. Upper part: excess heat power (right scale) and total input power (left scale). Lower part: measured ^{4}He in teratoms. Each point is the absolute quantity of ^{4}He in the sampling volume of 150 cm^3.

$d + d = {}^4\mathrm{He} + 23.8$ MeV (lattice) holds, by considering the measured heat excess, we calculated (see Appendix B) the amount of ^{4}He we had to expect at each sam-
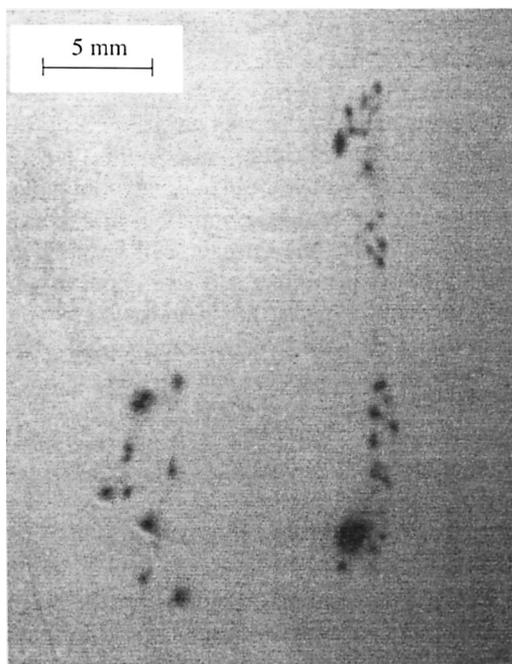

Fig. 13. X-ray film as obtained after an exposure of one week in front of cell #4.

pling of Fig. 12. Fig. 15 reports the results of this calculation with the excess heat power as in Fig. 12. The ratio between the measured and calculated ^{4}He, as reported in Fig. 16, is a parameter to check the energy balance. More specifically, the values of the ratio greater than 1 imply that the ^{4}He detected is of atmospheric nature (in this case, probably, because of incomplete washing) and/or heat excess is underestimated. On the other hand, from ~ 220 h until the end of the experiment, when the aforementioned ratio is steadily below unity, it is interesting to observe that there are several points definitely greater than zero and fairly close to the energy balance of the process.

The measurements performed on $^{20}\mathrm{Ne}^{2+}$ as a marker of contamination are affected by some uncertainties. Unlike the ^{4}He sensitivity that has been found to be extremely reproducible, 25 ± 3 pA/ppb or 7 ± 1 pA/Tat, during all the experiment, the $^{20}\mathrm{Ne}^{2+}$ apparent sensitivity was found to be scattered and decreased with time from ~ 2 to ~ 0.3 pA/Tat. Moreover, the amount of Ne detected has been always at the limit of detectability. The resulting measured ratios He:Ne, in spite of being generally greater than 0.29 (that of the air), are affected by a large error that, conservatively, prevented its use. The findings of our previous experiment, where a correlation was found between He and Ne even if the He/Ne ratios were greater than 0.29[14], must also be kept in mind; in the present experiment the very low range of values observed for the helium makes it difficult to look for the absence of such correlation.

Concerning the calorimetric results, they are, in terms of excess heat and highest ratio P_{exc}:P_{in}, 9.3 MJ and 0.8, respectively as, for instance, in the case of cell #4.

4.2. X-ray film

The following questions arise from the examination of Fig. 13 and Fig. 14. They are: (i) why is there an unexposed region in between the two distributions of spots? (ii) why are there spots? (iii) what is the energy of the radiation? (iv) how much is the total energy released? (v) what is the nature of the radiation?

(i) A highly symmetrical zone is clearly visible, without spots, around the axis at $X = 0$ of the film that could be reasonably attributed to the shadow (m in Fig. 5) produced by the 1-mm diameter Pt, ϕ_{Pt}, wire of the anode skeleton (see Fig. 5) and parallel to the Z-axis of the cathode. This is supported by the excellent agreement between the shadow width measured (7.00 ± 0.05 mm) and calculated according to the equation:

$$m = 2R_t\mathrm{inv}\sin\left[\frac{d}{R_t}\sin\mathrm{invtg}\left(\frac{\phi_{\mathrm{Pt}}}{2f}\right)\right] = 7.67 \text{ mm} \qquad (7)$$

by assuming the radiation source as point-like and localized in the Z-axis of the cathode. If we use the

Table 3
X-ray film data

Exposure (R)	Z/mm	X/mm	d_i/mm	t_i/mm	$w_i/sterad \times 10^4$	$\frac{\Phi_{s,i}}{\kappa_i} \times 10^2$
0.049	23.60	−7.00	0.48	50.39	0.70	0.84
0.030	23.00	−6.38	0.54	50.32	0.92	0.96
0.095	23.00	−6.93	0.54	50.38	0.92	0.96
0.095	22.40	−5.70	0.48	50.26	0.70	0.84
0.089	22.40	−6.38	0.54	50.32	0.92	0.96
0.049	22.40	−6.86	0.61	50.38	1.16	1.08
0.11	21.80	−5.77	0.82	50.27	2.07	1.44
0.049	21.80	−6.66	0.82	50.35	2.06	1.44
0.14	21.20	−5.31	0.95	50.23	2.82	1.68
0.082	21.20	−6.33	0.68	50.32	1.43	1.20
0.23	20.60	−5.28	0.88	50.22	2.43	1.56
0.037	20.60	−6.57	0.68	50.34	1.43	1.20
0.043	20.00	−5.30	0.48	50.22	0.70	0.84
0.069	20.00	−6.53	0.82	50.34	2.06	1.44
0.062	19.40	−6.44	1.40	50.33	5.73	2.39
0.024	18.80	−6.72	0.75	50.36	1.73	1.32
0.018	18.20	−6.86	0.61	50.38	1.16	1.08
0.043	17.60	−7.15	0.41	50.41	0.51	0.72
0.075	17.00	−6.66	0.88	50.35	2.42	1.56
0.082	16.40	−7.12	0.54	50.40	0.91	0.96
0.082	15.80	−6.49	0.48	50.34	0.70	0.84
0.075	15.80	−7.17	0.48	50.41	0.70	0.84
0.082	15.20	−7.03	0.68	50.39	1.43	1.20
0.12	10.20	3.97	0.95	50.13	2.83	1.68
0.082	10.20	−5.03	1.00	50.20	3.24	1.80
0.10	9.60	5.41	1.40	50.23	5.76	2.40
0.043	9.60	4.01	0.54	50.13	0.93	0.96
0.069	9.60	−4.79	1.00	50.18	3.24	1.80
0.14	9.00	5.57	1.60	50.25	8.29	2.88
0.082	9.00	−4.63	0.82	50.17	2.08	1.44
0.024	9.00	−5.22	0.82	50.22	2.07	1.44
0.024	8.40	5.77	1.50	50.27	6.96	2.64
0.069	8.40	−4.67	0.75	50.17	1.75	1.32
0.049	8.40	−5.47	0.61	50.24	1.17	1.08
0.024	7.80	6.05	0.68	50.29	1.44	1.20
0.062	7.80	−4.63	0.68	50.17	1.44	1.20
0.082	7.80	−5.55	0.82	50.25	2.07	1.44
0.12	7.20	6.21	0.75	50.31	1.74	1.32
0.075	7.20	−4.55	0.82	50.17	2.08	1.44
0.062	6.60	6.25	0.75	50.31	1.75	1.32
0.062	6.60	4.25	0.61	50.14	1.17	1.08
0.043	6.60	−4.71	0.68	50.18	1.44	1.20
0.082	6.00	4.37	0.75	50.15	1.75	1.32
0.089	6.00	−4.63	1.40	50.17	5.77	2.40
0.069	5.40	7.17	0.95	50.41	2.80	1.67
0.082	5.40	6.33	0.82	50.32	2.07	1.44
0.037	5.40	−4.55	0.54	50.17	0.92	0.96
0.043	5.40	−5.19	0.54	50.22	0.92	0.96
0.037	4.80	7.01	0.82	50.39	2.06	1.44
0.024	4.80	6.29	0.68	50.32	1.43	1.20
0.024	4.80	−4.15	0.95	50.14	2.83	1.68
0.062	4.20	5.37	1.50	50.23	6.97	2.64
0.056	4.20	−3.83	1.60	50.12	8.33	2.89
0.043	4.20	−4.79	0.68	50.18	1.44	1.20
0.12	3.60	5.37	1.40	50.23	5.76	2.40
0.17	3.60	−3.67	2.40	50.11	18.70	4.33
0.0061	3.00	5.01	0.68	50.20	1.44	1.20
0.20	3.00	−3.47	2.40	50.10	18.80	4.33
0.012	2.40	5.05	0.68	50.20	1.44	1.20
0.11	2.40	−3.43	1.50	50.09	7.00	2.65
0.069	2.40	−4.39	0.82	50.15	2.08	1.44

Table 3 (continued)

Exposure (R)	Z/mm	X/mm	d_i/mm	t_i/mm	w_i/sterad $\times 10^4$	$\frac{\Phi_{s,i}}{\kappa_i} \times 10^2$
0.037	1.80	5.53	0.82	50.24	2.07	1.44
0.12	1.80	−3.11	0.88	50.08	2.45	1.56
0.037	1.80	−4.39	0.41	50.15	0.52	0.72
0.089	1.20	5.57	0.82	50.25	2.07	1.44
0.037	1.20	3.97	0.95	50.13	2.83	1.68
0.14	0.60	4.13	1.30	50.14	5.22	2.28
0.0061	0.00	4.49	0.54	50.16	0.92	0.96
0.018	0.00	3.89	0.82	50.12	2.08	1.44

measured value of m to calculate the distance f, we obtain $f = 7.12$ mm. There is a deviation of 0.62 mm that is well explained by the deformation of the cathode observed at the end of the experiment.

(ii) The exposure of an X-ray film during an experiment involving energy of a few eV is very difficult to explain in terms of textbook science, so that nuclear phenomena necessarily have to be considered. In the present case, the spot nature further complicates the interpretation of this experimental evidence. As a working hypothesis, consider a primary process that produces directly or indirectly, photons sufficiently energetic to cross the cathode and all the materials in between it and the film. X-ray diffraction cannot be an explanation because the spot pattern, even if it were diffraction, the attenuation of the intensity, I/I_o, produce by all the materials, of photons at an average energy of the K_α lines of Pd (21.61 keV), would be total as calculated by the equation

$$I/I_0 = \exp\left[-\sum_i \rho_i (\mu/\rho)_i t_i \right] = \prod_i \exp[-\rho_i (\mu/\rho)_i t_i] \quad (8)$$
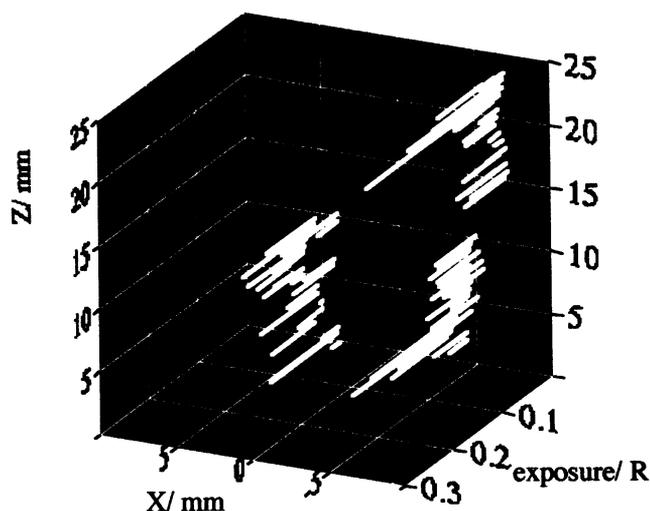

Fig. 14. Microdensitometry of the X-ray film. The X, Z plane (X-ray film plane) is quite parallel to the plane containing the longitudinal axis of the cathode. This is positioned 5 cm far from the film. Exposure is given in Roentgen (R).

and reported in Fig. 17. In Eq. (8), ρ is the density, (μ/ρ) is the mass absorption coefficient, which is a function of the photon energy, and t is the path length of the radiation in a given material i. The question is, what is the nature of the source? If the source were coherent, oriented and localized, the pattern found would have its own consistency but we do not have enough elements to support this. If the source were a conventional isotropic source, some reasonable explanations can be given in terms of physics of radiation. The first elementary consideration is that the source site is not at the surface of the cathode because a diffuse blackening instead of spots would be expected in this case. Consequently, the shape of the cathode becomes important. In the present case, the cathode is bundle shaped and it can be satisfactorily represented by a packing of seven shells of wires as reported in Fig. 18. For the sake of simplicity, we assume the source is located in the centre of the system. It is easy to verify that the effective path length of the radiation in the Pd wires depends upon the angle of propagation. For a point-like source, the minimum and the maximum are attained, respectively, for the (a) and (b) paths reported in Fig. 18. In this framework, the system can be described as a system of virtual slits seen as domains in the space where the attenuation, I/I_0, is relatively low according to Eq. (8). In the present experimental set-up, the value of Eq. (8) depends only on the photon energy and the position of the source in the cathode, i.e., it depends on the effective path length, t, in Pd. By inspection of Fig. 17, it is quite evident that a fixed energy, the transmission is greatly influenced by t, at least up to 150 keV. As an example, Fig. 19 shows the quantity I/I_0 calculated against the angle of propagation of the radiation (details of this calculation are given in Appendix C). Here the source is supposed to be point-like, localized in the centre of two wires having coordinates (0, 0) and [(433.01, 750)-4th shell] and, the emitted radiation, confined, for simplicity, only in a thin slice orthogonal to the z-axis passing in the coordinate origin of Fig. 18. It is shown in Appendix C that the t vs. α pattern can be greatly modified when the source is moved out of the centre of a wire. In principle, the source or sources can be everywhere, but we

Table 4
Results of the determination of ^{4}He in some cut sections of the cathode of cell #4

Cell #4 # Section	Weight/mg	D_2/pA	Valley/pA	^{4}He/pA	^{4}He/Tat	Remark
1	550	13 000	3	10		NR
2	1337					NY
3	621	1000	1	3	0.4	
4	751					NY
5	267					NY
6	347	100 000	200	400		NR
7	355					NY
8	351	16 000	7	17		NR
9	387					NY
10	422	13 000	4	12		NR
11	513	950	3	3	0.4	
12	533	1000	2	2	0.3	
13	1270	50 000	30	50		NR
14	317	27 000	190	360		NR

can conclude that they are not at the surface of the outermost wires of the bundle because no diffuse blackening of the film was observed. Therefore, the sources have to be inside the innermost wires or at their surfaces. The spots represent the shortest paths of the radiation within the Pd wires (likely at 60°) produced by the sources located at different positions along the Z-axis of the bundle. Concerning their position on the Z-axis of the film (Fig. 14), it is important to be reminded that in the real system, the bundle cathode, there is a slight rotation around its own Z-axis (see Section 2), strongly increasing the attenuation of the radiation in the direction out of the X, Y plane (see Fig. 18) of the bundle. By examination of Table 3, one finds that in some cases more than one spot is positioned at the same Z value. This could mean that more than one source is located in the same plane orthogonal to the major axis of the bundle. The direction where the intensity of the radiation propagation is the most intense would be shifted on the X-axis of the film according to the torsion of the bundle.
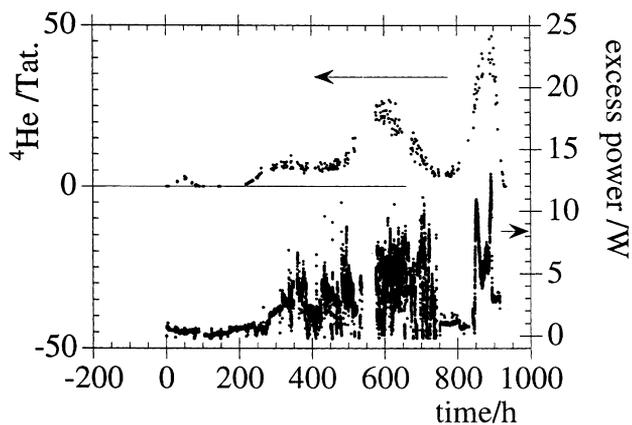

Fig. 15. Calculated ^{4}He (lefthand scale) and heat power excess (righthand scale).

In the present assumption of isotropic radiation, the dimensions of a spot on the film may depend of the line shape of the attenuation of the radiation with respect to the sensitivity of the film. To be clearer, if the film were ultrasensitive, we probably would not observe any spot but more likely a diffuse blackening of the film due to the superimposition of halos. Since the shape of the spots on the film appears to be quite circular, it is reasonable to assume that for each spot i, the angular components, azimuthal ω_i and equatorial ϑ_i, of the solid angle, w_i, are equal. They are given by the equation:

$$\omega_i \cong \varphi_i \approx w_i^{1/2} = \left(\frac{\pi d_i^2}{4t_i^2}\right)^{1/2} \tag{9}$$

The terms d_i and t_i are presented in Table 3 and they are, respectively, the measured diameter of the spot and the optical path of the radiation calculated according to quation:

$$t_i = \frac{R_t \sin \Omega_i}{\sin\left[\text{inv tan}\dfrac{R_t \sin \Omega_i}{d - R_t(1 - \cos \Omega_i)}\right]}; \quad \Omega_i = \frac{l_{t,i}}{2R_t} \tag{10}$$

In the above equation, $l_{t,i}$ is the value of the X coordinate of a spot measured in the film from the central axis of the spot distribution. This axis has been arbitrarily placed at $l_{t,\max}/2$ where $l_{t,\max}$ is the horizontal distance between the leftmost and rightmost spots in the film. The values of $\omega_i = \vartheta_i$ range from 0.41 to 2.48° with a statistical distribution whose most probable value is at (0.75 ± 0.25)°. It is important to observe that the values obtained for ω_i or ϑ_i do not depend on the model of the *virtual slit* here used and they hold even if we were dealing with oriented and coherent sources. In this case, each spot would be the image of its own source. Thus, it is interesting to try a calculation of the source size, $\Phi_{s,i}$. This quantity is obtained by the equation:
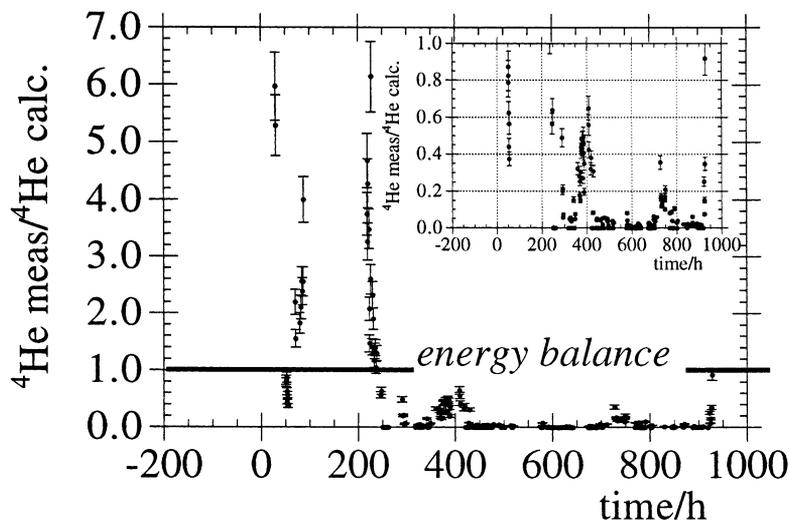
Fig. 16. Ratio between measured and calculated ^{4}He vs. time. The inset is a magnified view in the range from 0 to 1.

$$\Phi_{s,i} = 2\kappa_i \tan\left(\frac{\Phi_i}{2}\right) \tag{11}$$

where κ_i is the distance of the source from the origin of the coordinate system and ϑ_i is given by Eq. (10). In Table 3 the $\Phi_{s,i}/\kappa_i$ value calculated according to Eq. (11) is reported. No direct possibility exists to evaluate κ_i. It is, however, interesting to observe that the sources could have dimensions comparable with the size of the grains, or the grains themselves could be the sources. If the values of $\Phi_{s,i}/\kappa_i$ are multipled for $\kappa_i \approx 2500$ μm, one obtains a $\Phi_{s,i}$ distribution centred at 35 ± 5 μm comparable to the grain size distribution obtained by the metallography (see Section 2). This is well represented in Fig. 20. This result would be in agreement with coherent sources localized in the grains at the surface of the outermost wires of a real bundle cathode. A value of $\kappa_i \approx 2500$ μm implies ≈ 5000 μm for the diameter of the cathode. This value is very close to the diameter of the cathode measured at the end of the experiment.

(iii) To make an estimation of the energy of the radiation detected, the following justification can be done: (a) Eq. (8) is rewritten in the form

$$I/I_0 = Q \exp[-\rho_{Pd}(\mu/\rho)_{Pd}t_{Pd}] \tag{12}$$

where $Q = \Pi_i \exp[-\rho_i(\mu/\rho)_i t_i]$ being the Q term independent on the position of the source, and practically equal for all the spots in the film; (b) each spot is related to the same type of elementary event and the intensity of a spot depends on the radiation path length in the cathode, i.e., I_0 is always the same; (c) the most intense spot is associated with a source closer to the film, i.e., the source is in an outermost wire of the bundle, but not in the last shell (see above); (d) similarly, the weakest spot is related to the source that is
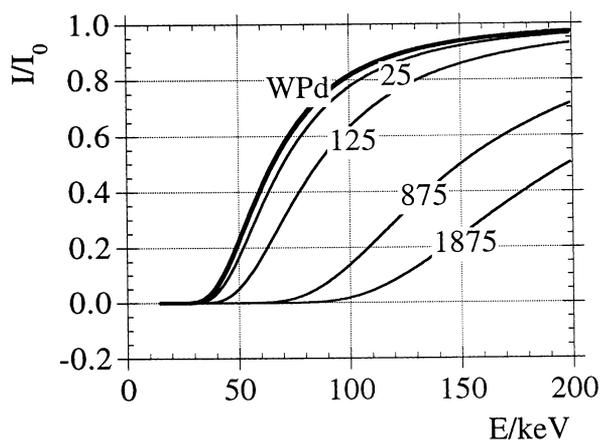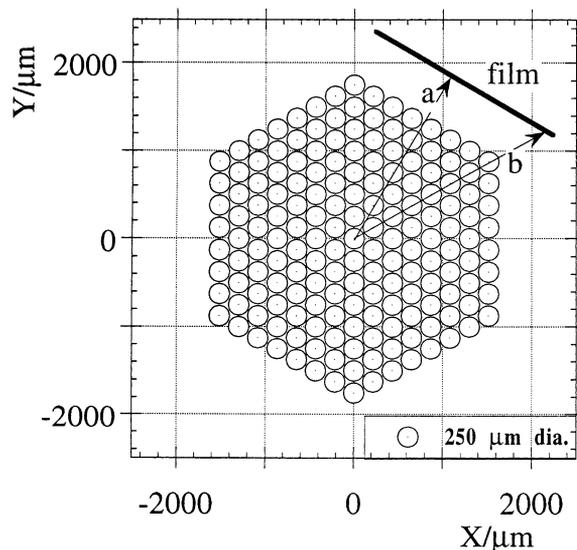

Fig. 17. Attenuation I/I_0 vs. photon energy of Pd given by the materials between the cathode and film (WPd = Without Pd) at different thickness (in μm) of Pd crossed.

Fig. 18. Representation of the cross-section of a bundle-type cathode as an ideal 7-shell packing with 169 wires of 250 μm diameter. The cathodes used were made of 150 wires.
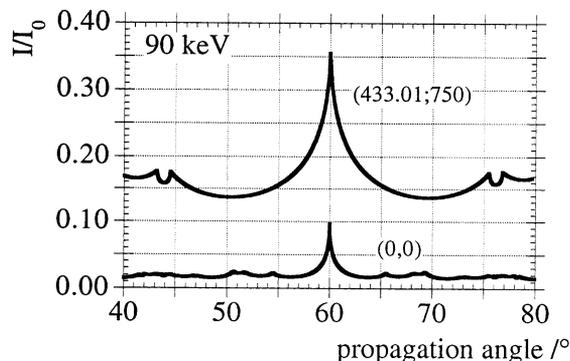
Fig. 19. Calculated transmission at 90 keV at two different positions of the source in the cathode.

the most distant from the film. From the ratio between $\frac{I_{min}/I_0}{I_{max}/I_0}$ and by Eq. (12), the value of the mass absorption coefficient, (μ/ρ), of Pd is obtained.

The dependence of (μ/ρ) on the photon energy [24] fits very well with the equation $(\mu/\rho) = aE^{-b}$, with $a = (3.10 \pm 0.05) \times 10^5$ cm^2 g^{-1} and $b = 2.676 \pm 0.004$. Combining the equations, the energy is found by equation:

$$E = \left[\frac{1}{a\rho_{Pd}(t_{min} - t_{max})} \ln \frac{I_{max}}{I_{min}} \right]^{-1/b} \quad (13)$$

In the above hypotheses, t_{max} and t_{min} have to be selected among the optical paths in Pd, which fall in the angle α (Fig. 5) corresponding to the maximum distance between spots in the film at $Z =$ constant (see Fig. 11). This angle was measured to be 16.3°. The source position has to be selected, respectively, on the surface of any wire in the 6th shell with centre coordinates [$0 \leq x_i \leq 1299$; $750 \leq y_i \leq 1500$] μm and in any wire belonging to the 6th shell with centre coordinates [$-1299 \leq x_i \leq 0$; $-1500 \leq y_i \leq -750$] μm. For symmetry reasons, the most appropriate values for t_{max} and
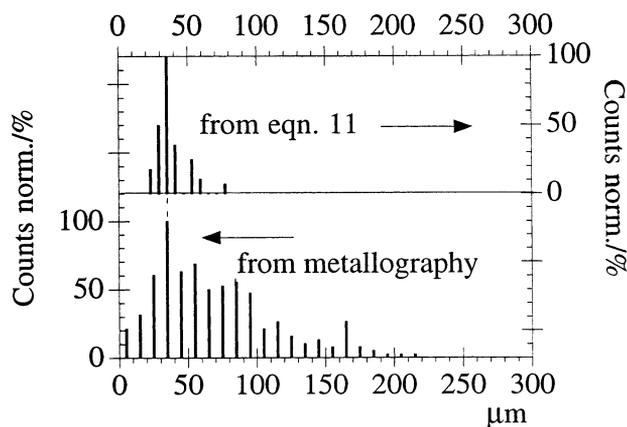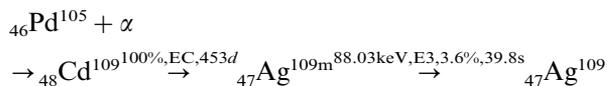

Fig. 20. Comparison between the grain distribution obtained by metallography and the distribution of the source size.

t_{min} are, 250 (the source is at the surface of a wire in the 6th shell) and 1875 μm (the source is in the origin of the system), respectively. As a consequence, by Eq. (13), the energy was calculated to be 89 keV. The systematic error on E is evaluated to be 1 keV by considering the error on the fit constants and the experimental error on the intensities that was less than 2%. The calculated value of the energy is probably underestimated because the highest possible value of t_{min} could be up to two times the value selected before. This would imply an energy around 120 keV. On the other hand, if the sources were assumed to be positioned at $\kappa_i \approx 2500$ μm, as discussed before, $(t_{min} - t_{max})$-2κ_i in Eq. (13), and the energy value would be equal to 135 keV.

(iv) At this point, the energy released by the process generating the radiation can be calculated because I_0 can be obtained from Eq. (12). The term Q is represented as a function of energy in Fig. 17, curve WPD and all the other terms are known. Therefore, per unity of solid angle, I_0 is $(4.0 \pm 0.1) \times 10^4$ R. Since the average density, $\bar{\sigma}$, of spots in the film is known, the quantity $\bar{\sigma}d^2 = 2750$ sterad^{-1} is the density of spots per unity of solid angle and the total energy of 4π sterad associated to the radiation is $4\pi k\bar{\sigma}d^2 I_0 = 12.0 \pm 0.4$ kJ (the conversion 1 $R = 87.8 \times 10^{-7}$ J $= k$ has been used). this energy is $\approx 0.5\%$ of the energy measured by calorimetry in the same interval of time during which the film was exposed.

(v) Looking at the energy of the K_α lines vs. the atomic number of the elements, the energy found is close to the energy of the K_α lines of Pb or Bi. Considering further that the energy evaluated is probably underestimated, we should look at the K_α lines of actinides. Since the chemical analysis did not detect Pb and Bi, and the presence of actinides is quite improbable, the emission on atomic basis cannot be invoked, and the nuclear origin of the radiation detected reasonably takes place. A working hypothesis, to find an explanation for this, could be found on the following nuclear process [25]:

$$_{46}Pd^{105} + \alpha$$

$$\rightarrow _{48}Cd^{109} \overset{100\%,EC,453d}{\rightarrow} _{47}Ag^{109m} \overset{88.03keV,E3,3.6\%,39.8s}{\rightarrow} _{47}Ag^{109}$$

where the stable isotope 105 of Pd (natural abundance 22.33%) capture the α's, produced by the d,d fusion, generating the Cd isotope 109. This nuclide is unstable and by electron capture transforms with a halftime of 453 days in the metastable isotope 109 of Ag. The transition to the stable isotope of Ag occurs through γ emission at 88.03 keV from a E3 state with a yield of 3.6% and a halftime of 39.8 s. This scheme would be consistent with the above findings provided the cross-section of the α's for Pd^{105} were sufficiently high.
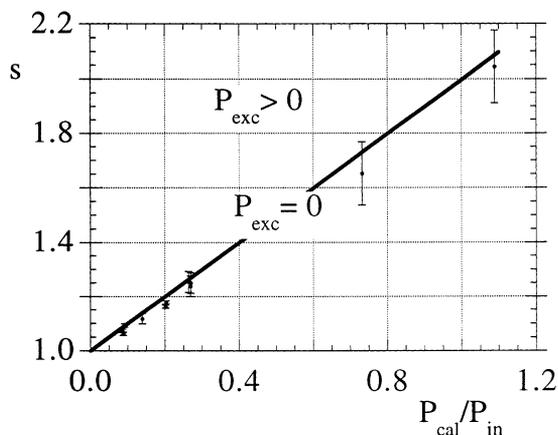
Fig. 21. Test of Eq. (2A) for the blank cell.

Fig. 22. Qualitative scheme to clarify the basis of the ^{4}He calculation by the calorimetric measurements.

5. Conclusions

The results show an overall picture with its own internal consistency: ^{4}He is produced at the surface of the wires, but only the innermost wires in the bundle are active (see the discussion about the spots on X-ray film) and it is not found inside Pd. On the other hand, the low levels of ^{4}He do not give the necessary confidence to state definitely that we are dealing with the fusion of deuterons to give ^{4}He. No evidence of contamination by atmospheric ^{4}He was found by the detection of ^{20}Ne^{2+}, and the energy balance seems quite well satisfied when ^{4}He, expected by the measured heat excess, is compared with ^{4}He found. This results markedly overcomes the stagnant situation in the understanding of cold fusion phenomena, where heat excess measured was never counterbalanced by a proper number of nuclear particles, such as neutrons, as expected by the d, d fusion in plasma. Moreover, the exposure of the X-ray film is a clear-cut proof (very simple experimental device for which errors of measurement and/or of procedure, as well as artefacts cannot be invoked) that a nuclear phenomenon is at work. We believe that the radiation detected has to be searched for among the stable isotopes of Pd or among its impurities having intense nuclear transitions close to the energy found. Work is in progress to check this route.

Appendix A

At times $t > \tau$ after the heater pulse is switched on, the energy balance of the flow calorimeter, according to Eq. (1), is written before, i, and after, f, as:

$$\frac{P_{el} + P_{exc} - P_{out,i}}{_i\Delta\vartheta_{wj,\infty}} = \frac{P_{el} + P_{exc}P_{cal} - P_{out,f}}{_f\Delta\vartheta_{wj,\infty}} \quad (1A)$$

from which

$$P_{exc} = \frac{1}{s-1}(P_{cal} + sP_{out,i} - P_{out,f}) - P_{el} \quad (2A)$$

where $P_{out} = P_{sg} + P_{rad}$ and $s = \frac{_f\Delta\vartheta_{wj,\infty}}{_i\Delta\vartheta_{wj,\infty}}$. P_{out} is always an increasing function of the temperature of the electrolytic solution, ϑ_s, and in order to $P_{exc} > 0$, the condition $(sP_{out,i} - P_{out,f}) > [(s-1)P_{el} - P_{cal}] > 0$ has to be satisfied. Fig. 21 shows the experimental test of the condition before for the blank cell.

Appendix B

The experimental behaviour observed (Fig. 7) in the transfer of a *parcel* of ^{4}He from the cell to the QMS is well-fit by the function:

$$x_{He} = at^5 e^{-bt}; \quad a = (7 \pm 1) \times 10^{-8} \text{ ppb s}^{-5},$$

$$b = (2.68 \pm 0.06) \times 10^{-2} \text{ s}^{-1}, \quad R = 0.97704 \quad (1B)$$

where t is the time in seconds. The maximum of ^{4}He concentration can be detected only if the MS measurement is done after t_{max} s from the ^{4}He generation inside the cell. For the sake of clarity, consider Fig. 22 where

some generations of ^{4}He occur at the times $t_{p_0}, t_{p_1}, t_{p_2}, \ldots, t_{p_i}$. In our experimental situation, these times represent the times when we measured P_{exc} by calorimetry. At the times $t_{s_0}, t_{s_1}, t_{s_2}, \ldots, t_{s_i}$, the samplings were done to perform the ^{4}He measurement. The gas mixture sampled is the mixture passed in the sampling cylinder $\Delta t_0, \Delta t_1, \Delta t_2, \ldots, \Delta t_i$ s before the respective times $t_{s_0}, t_{s_1}, t_{s_2}, \ldots, t_{s_i}$. Therefore, Δt_i is the time necessary to fill the sampling volume V_s by the mixture moving at the flowrate $q_m[I(t_{p_i})]$ see (see Eq. (6)) which depends on the electrolysis current at the time t_{p_i}. Thus Δt_i is the *time window* where ^{4}He is measured. It is given by:

$$\Delta t_i = \frac{PV_s}{KT q_m[I(t_{p_i})]} \tag{2B}$$

The ^{4}He atoms present in Δt_i represent the summation of all the contributions of the past ^{4}He generations. It is clear that the atoms ^{4}He atoms sampled at t_{sj}, $N_{t_{sj}}$ depends on the time and intensity generating patterns provided the samplings are performed at constant intervals.

The whole reasoning can be cast in the equation below as:

$$N_{t_{sj}} = ag \sum_{i=0}^{m} q_m[I(t_{p_i})] \int_{t_{sj}-\Delta t_i}^{t_{sj}} (t - t_{pi})^5 e^{[-\beta_i(t - t_{pi})]q} \, dt \tag{3B}$$

where the summation is extended to the mP_{exc} measurements occurring to the times $t_{pi} \le t_{sj} - \Delta t_i$. The constant g has value depending on the unity of measure chosen. The propagation function given in Eq. 1B has to be modified for considering that the time origin is shifted, with respect to Eq. 1B itself and Fig. 7, by the quantity t_{p_i} and the constant b has to be normalized with respect to the number of ^{4}He atoms used in the propagation experiment.

It is known [26] that $\int_0^\infty x^n e^{-bx} \, dx = \frac{n!}{b^{n+1}} \xrightarrow{n=5} \frac{120}{b^6}$. This implies that $N_{He} = agq_m \int_0^\infty t^5 e^{-\beta_i t} \, dt = agq_m \frac{120}{\beta_i^6} = z \int_{t_{P_i}}^{t_{pi+1}} P_{exc} \, dt$. Therefore, β_i is calculated through the equation:

$$\beta_i \left(\frac{120 agq_m}{z \int_{t_{pi}}^{t_{pi+1}} P_{exc} \, dt} \right)^{1/6}; \quad z = \frac{q_r}{N_A g} \tag{4B}$$

where $q_r = 2.63 \times 10^{11} \text{ W}^{-1} \text{ s}^{-1}$ is the number of ^{4}He atoms associated with 1 J of energy generated by the d, d nuclear reaction.

Appendix C

To evaluate the attenuation of the radiation produced by a multishell system like that reported in Fig. 18, it is necessary to calculate the t term in Eq. (8) by the summation of all the paths, r_i, the radiaton through the Pd wires when it propagates according to a given angle α. Therefore, supposing the radiation originating in the source localized at the coordinates $[x_0, y_0]$ r_i represents the length of the secant produced by the oriented straight-line (propagation of the radiation from the source to the film)

$$y - y_0 = (x - x_0)tg\alpha \tag{1C}$$

which intersects the circle (the cross-section of the Pd wire in the X, Y plane)

$$(y - y_i)^2 + (x - x_i)^2 = \frac{d_w^2}{4}, \tag{2C}$$

where $[x_i, y_i]$ are its centre coordinate sand d_w is its diameter. Combining the previous equations in a system, the distance between the intersection points produced by the line with the circle, is

$$r_i = 2[(A_i^2 - C_i)(1 + tg^2\alpha)]^{1/2} \tag{3C}$$

where

$$\begin{cases} A_i = \dfrac{[(y_0 - x_0 tg\alpha - y_i)tg\alpha - x_i]}{1 + tg^2\alpha} \\ C_i = \dfrac{(y_0 - x_0 tg\alpha - y_i)^2 + x_i^2 - \dfrac{d_w^2}{4}}{1 + tg^2 A} \end{cases} \tag{4C}$$

In order that the intersection occurs $A_i^2 - C_i > 0$ has to be fulfilled. The terms of r_i to be considered in the summation for evaluating t have to be only those terms which concur with the orientation of the line of propagation of the radiation. To fulfil this requirement, the following restrictions have to be considered:

$$\begin{cases} x_{i,P} > x_0 + \dfrac{d_w}{2}\cos\alpha \\ y_{i,P} > y_0 + \dfrac{d_w}{2}\sin\alpha \end{cases} \tag{5C}$$

where $-A_i - (A_i^2 - C_i)^{1/2} = x_{i,P} < x_{i,Q} = -A_i + (A_i^2 - C_i)^{1/2}$ and $[(x_{i,P} - x_0)tg\alpha + y_0] = y_{i,P} < y_{i,Q} = [(x_{i,Q} - x_0)tg\alpha + y_0]$ hold for the intersection condition. $[x_{i,P}, y_{i,P}]$ and $[x_{i,Q}, y_{i,Q}]$ are the coordinates of the intersection points of the propagation straight-line with the circle. Fig. 23 gives the trend of t vs. α for just two of the infinite point-like sources present, in principle, in the system of Fig. 18. Fig. 23 also shows $_c$ in the case where we consider a continuous system instead of a bundle system having the same external dimensions. In this case, $t_c = (x_{i,Q} - x_0)(1 + tg^2\alpha)^{1/2}$ where the restrictions Eq. (5C) still hold. It clearly appears that the position of the source greatly influences the t_b pattern whereas t_c pattern is practically unaffected. The virtual
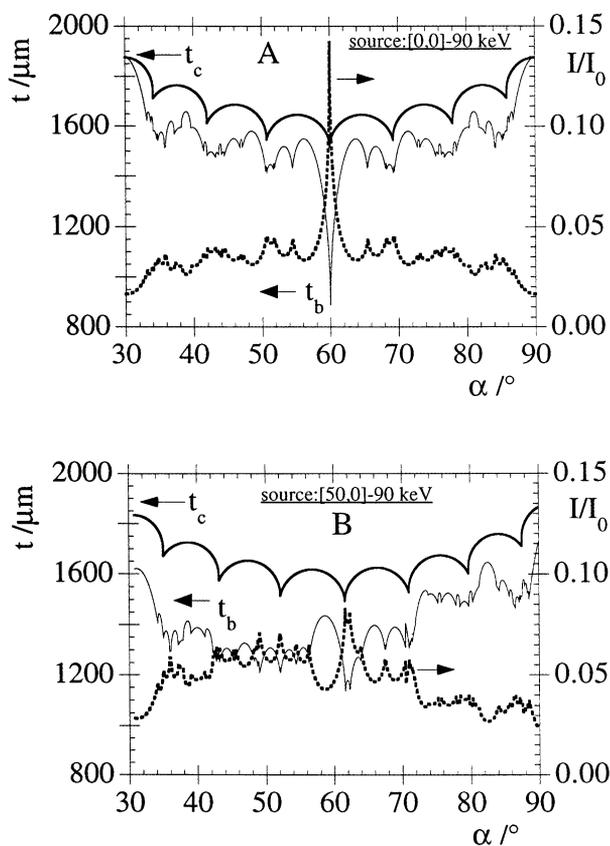
Fig. 23. Trend of the radiation path length as a function of the angle, α, of the radiation propagation in a 7-shell packing of 250 μm diameter wires. t_c and t_b are the geometric distance between the source and the contour, and the distance the radiation would travel in Pd, respectively. On the righthand scale is the attenuation I/I_o. (A) source located in the centre [0, 0] of the wire in the origin of the system, (B) source located in the same wire but 50 μm [50, 0] shifted in the positive direction of X-axis.

slit concept is particularly well represented in Fig. 23A at $\alpha = 60°$.

Appendix D. Glossary of the symbols and their units

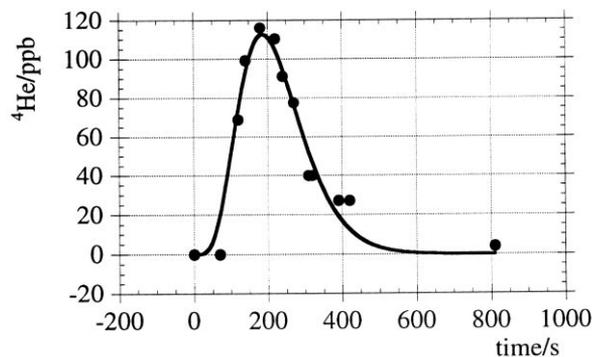|		
c_1	J mol^{-1} °C^{-1}	Heat capacity of H_2O (1): [75.260]
Cg	J mol^{-1} °C^{-1}	Heat capacity of D_2O (g): [44.500]
C_1	J mol^{-1} °C^{-1}	Heat capacity of D_2O (1): [84.349]
d	m	Distance between the centre of the cathode and the X-ray film
d_w	m	Pd wire diameter: [(2.50 or 5.00) × 10^{-4}]
E	keV	Energy of the radiation
f	m	Distance between the vertical axes of the cathode and a Pt wire of the anode skeleton
F	C mol^{-1}	Faraday constant: [96484.6]
I	A	Electrolysis current
I_h	A	Current applied to the heater
I/I_0		Attenuation of a beam of photons
k_{rad}	J K^{-4} m^{-2}	Stephan-Boltzman constant: [5.6703 × 10^{-8}]
$l_{t,i}$	m	X-coordinate of a spot measured on the film
m	m	Shadow width measured on the film
n		Number of samplings
p	bar	Vapor pressure of D_2O: [7.83 × 10^{-3} exp(5.143 × 10$^{-2}\vartheta_s$)
P	bar	Total pressure in the cell: [2.25]
P_{cal}	W	Heat power generated at the calibration step
P_{el}	W	Electric power to carry out electrolysis
P_{exc}	W	Heat power excess
P_{in}	W	Total input power to the cell
P_{rad}	W	Power radiated from the cell to the bath
P_{sg}	W	Power to saturate the gas stream with D_2O vapor
P_w	W	Power exchanged by the water stream in the water jacket
q_{H_2O}	m^3 s^{-1}	Flow rate of the water stream in the water jacket
q_{N_2}	std cm^3 min^{-1}	Flow rate of the protective nitrogen stream: [40]
q_m	std cm^3 min^{-1}	Flow rate of the gas mixture
q_r	W^{-1} s^{-1}	Number of ^{4}He atoms associated with 1 J generated by the d, d fusion reaction: [2.63 × 10^{11}]
r_v		Ratio between the volume of gas mixture of n samplings and the total volume of the gas mixture in the experiment
R_t	m	Radius of torus: [0.25]
S_s	m^2	Radiating surface area: [2.4 × 10^{-2}]
t_i	m	Path length of the radiation
v_{wj}	m^3	Volume of the water contained in the water jacked: [$\sim 6 \times 10^{-5}$]
V_a	m^3	Volume of the gas mixture of n samplings
V_e	m^3	Volume of the gas mixture produced throughout the experiment
V_h	V	Voltage measured across the heater
V_{in}	V	Voltage measured across the electrodes of the electrolysis cell

Fig. 7. Propagation of a *parcel* of ^{4}He in the line extending from the cell to the sampling cylinder after an injection in the cell of 10 scc of air (1.27×10^{15} ^{4}He atoms). Carrier gas flow rate = 40 sccm.

crucible. The standard procedure adopted here consists of heating the crucible over the m.p. of Pd (1552°C) under high-vacuum pumping; then, after closing the gate valve, make the samples fall into the crucible while increasing the temperature above 1650°C, and maintaining this temperature for at least 10 min. Finally a rapid cooling follows. At the same time, the evolved gases are allowed to be gettered, first in a LN$_2$ charcoal trap and, subsequently, by 57-707 SAES getters. Finally, when the pressure in the system decreases below 2×10^{-5} mbar, the QMS is connected and the measurement is carried out in MID mode.

3. Results

Figs. 9–12, for cells 1 to 4, respectively, show in the upper panels the total input power supplied to the cell
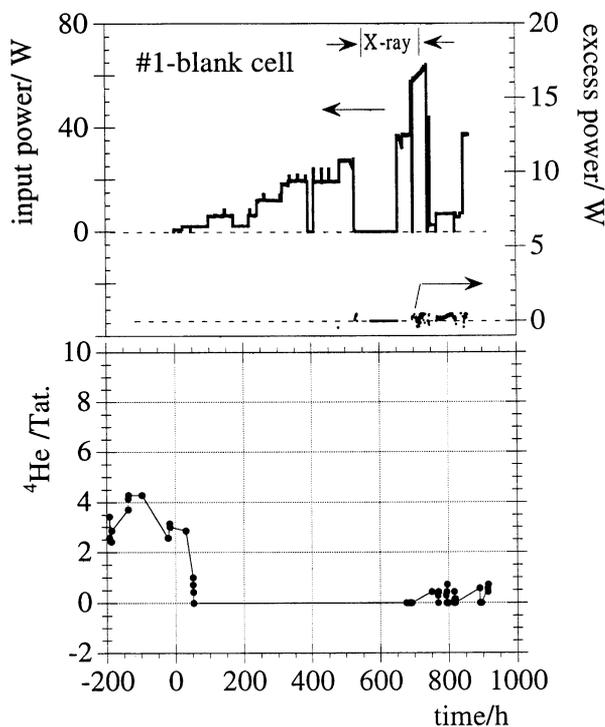

Fig. 9. Cell # 1 (blank). Cathode made of a bundle of 1 mm diameter Pt wires. Upper part: excess heat power (right scale) and total input power (left scale). Lower part: measured ^{4}He in teratoms. Each point is the absolute quantity of ^{4}He in the sampling volume of 150 cm^3.

(lefthand scale) and the time patterns for the excess heat power (righthand scale). The measured absolute quantity of ^{4}He in teratoms (10^{12} atoms) is given in the lower panels of each figure. The instability of the flow rate of the cooling water in some periods of the experiment prevented reliable data of excess heat power being
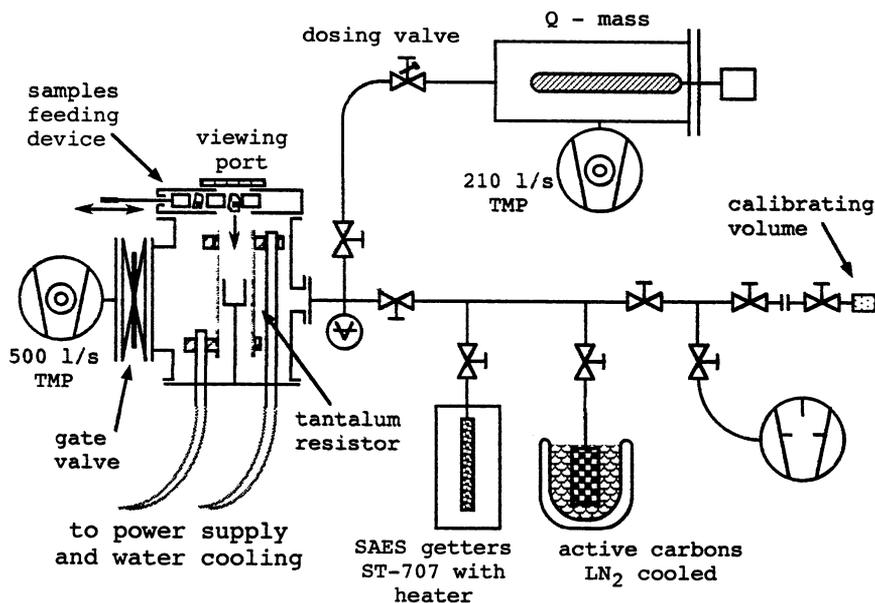

Fig. 8. Scheme of the apparatus for determining ^{4}He inside the cathode.